

# High irradiance performance of metal halide perovskites for concentrator photovoltaics

Zhiping Wang<sup>1,2</sup>, Qianqian Lin<sup>1,2</sup>, Bernard Wenger<sup>1</sup>, M. Greyson Christoforo<sup>1</sup>, Yen-Hung Lin<sup>1</sup>, Matthew T. Klug<sup>1</sup>, Michael B. Johnston<sup>1</sup>, Laura M. Herz<sup>1</sup> and Henry J. Snaith<sup>1\*</sup>

**Traditionally, III–V multi-junction cells have been used in concentrator photovoltaic (CPV) applications, which deliver extremely high efficiencies but have failed to compete with ‘flat-plate’ silicon technologies owing to cost. Here, we assess the feasibility of using metal halide perovskites for CPVs, and we evaluate their device performance and stability under concentrated light. Under simulated sunlight, we achieve a peak efficiency of 23.6% under 14 Suns (that is, 14 times the standard solar irradiance), as compared to 21.1% under 1 Sun, and measure 1.26 V open-circuit voltage under 53 Suns, for a material with a bandgap of 1.63 eV. Importantly, our encapsulated devices maintain over 90% of their original efficiency after 150 h aging under 10 Suns at maximum power point. Our work reveals the potential of perovskite CPVs, and may lead to new PV deployment strategies combining perovskites with low-concentration factor and lower-accuracy solar tracking systems.**

For mainstream utility-scale PV, the module cost has dropped to less than half the cost of the total PV installation. This makes strategies that raise the module efficiency increasingly important, because an increased power output per square metre of deployed PV offsets the balance of systems costs, which predominantly scale with area. The economic pressure to deliver higher power output per square metre is also making more expensive deployment strategies feasible, such as solar tracking for flat-plate technologies<sup>1,2</sup>. As the fraction of global electricity generation from PV increases, it will become increasingly important to spread the temporal profile for PV electricity generation as broadly as possible throughout the day. With the latter consideration, two-axis solar tracking, where the PV modules point directly towards the Sun from dawn to dusk, should become increasingly popular. If we anticipate that sensible two-axis solar tracking strategies will be developed and become economically viable through manufacturing and deployment scaling, we should consider high-efficiency PV concepts that work best under direct sunlight as a feasible option for next-generation PVs. CPV is a technology-agnostic approach toward increasing power conversion efficiency (PCE). In CPV configuration, sunlight is focused onto a small area using lenses (or parabolic mirrors as concentrating optics<sup>3</sup>), which we illustrate in Fig. 1. The increased light intensity results in a higher density of photo-generated carriers, which drives a larger quasi-Fermi-level splitting in the semiconductor absorber material (Fig. 1d), delivering a higher output voltage and hence increased PCE of the cells<sup>3</sup>. Commercial CPVs are multi-junction cells based on III–V semiconductors<sup>4,5</sup>. The highest PCE previously obtained for a CPV cell is 46% for a four-junction GaInP/GaAs/GaInAsP/GaInAs under 508 Suns irradiance, whereas a similar five-junction cell achieves 38.8% under 1 Sun illumination<sup>6</sup>. The reason that it has been feasible to use the III–V multi-junction technology in CPV applications is that the active cell area is small in comparison to the total area of the module capturing sunlight, enabling the high cell cost to be accommodated in the overall cost of the deployed PV array<sup>7</sup>. However, this does set considerable demands on the solar tracking and concentrating optics, increasing their cost. A conflicting challenge to deliver a

highly cost competitive CPV solution has arisen<sup>7</sup>. At present, owing to the continuing downward drive in the price for conventional PV, III–V multi-junction CPVs are struggling to compete with the scale of growth occurring with flat-plate PV technologies<sup>2</sup>.

Development of low-cost and high-efficiency materials for CPV applications, which could allow for less stringent solar tracking and concentrating optics, could reset the cost competitive balance. In recent times, low concentrator factors, of the order of 10- to 100-fold, have been investigated for high-efficiency silicon cells<sup>2,8</sup>. Thus far, the cost balance has not made this favourable over conventional flat-plate deployment strategies, presumably because the energy generation gains have not outweighed the additional costs. This suggests that efficiencies greater than those currently achieved with single-junction Si PV, combined with cell costs which are no more expensive than for Si, will be necessary to make the economics feasible for low-concentration factor CPV.

Photovoltaics based on metal halide perovskites have recently emerged as an interesting option that combines high efficiency and low cost<sup>9–11</sup>. Single-junction cells have achieved efficiencies over 22%<sup>12,13</sup>, and tandem cells constructed by combining perovskite top cells with silicon have achieved efficiencies over 26%<sup>14,15</sup>. Beyond the performance already demonstrated in laboratories, we have estimated that it will be feasible for perovskite solar cells to surpass 38% efficiency when measured under 1 Sun illumination, when integrated into a triple-junction architecture<sup>16</sup>. By combining perovskite multi-junction cells with silicon PV and delivering much higher efficiencies, we may be able to tip the economics in favour of low-concentration CPV for large-scale deployment.

Perovskite solar cells are capable of sustaining linearity in photocurrent generation up to intensities of many tens of Suns<sup>17–20</sup>. However, increased efficiency under increased light intensity is yet to be demonstrated. Another key consideration for CPV applications is the intrinsic material stability to intense sunlight, where any light-induced degradation is expected to be accelerated proportionally to the solar concentration factor. Early stability measurements on perovskite solar cells exhibited fast degradation under 1 Sun illumination<sup>21,22</sup>, but recent advances in perovskite composition and

<sup>1</sup>Clarendon Laboratory, Department of Physics, University of Oxford, Oxford, UK. <sup>2</sup>These authors contributed equally: Zhiping Wang, Qianqian Lin. \*e-mail: [henry.snaith@physics.ox.ac.uk](mailto:henry.snaith@physics.ox.ac.uk)

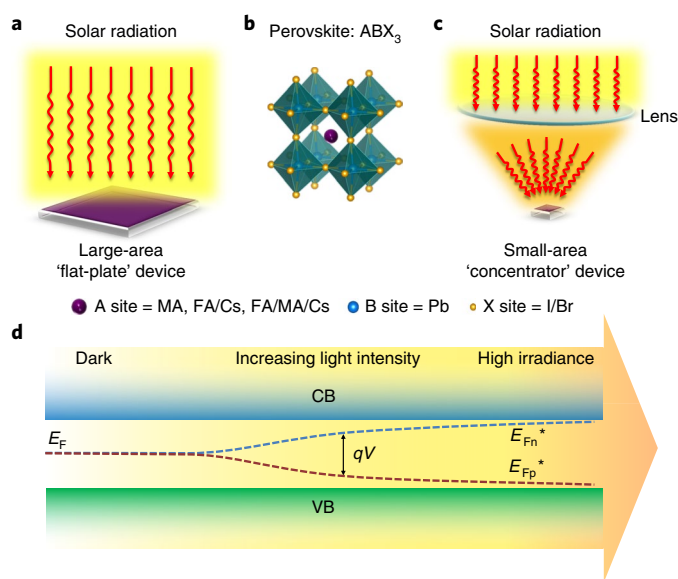


**Fig. 1 | Perovskite-based concentrator photovoltaics.** **a**, Large-area, ‘flat-plate’ perovskite solar cell devices operated up to 1 Sun irradiance. **b**,  $ABX_3$  perovskite crystal structure. MA, FA and Cs stand for methylammonium ( $CH_3NH_3^+$ ), formamidinium ( $(NH_2)_2CH^+$ ) and caesium, respectively. **c**, Perovskite CPV devices. The normal 1 Sun irradiance is concentrated onto a small-area perovskite solar cell by a focusing lens or a parabolic mirror (not shown here), which delivers a higher power output. **d**, Schematic illustration of the Fermi level splitting in a solar absorber material with increasing light intensity.  $E_f$  represents intrinsic Fermi level.  $E_{Fn}^*$  and  $E_{Fp}^*$  are the quasi-Fermi levels for electrons and holes respectively, where light absorption results in electrons populating the conduction band (CB) and holes populating the valence band (VB).

device architecture have led to considerable improvements in long-term operational stability<sup>14,23,24</sup>. We recently theoretically assessed the prospects of perovskite PV cells under high irradiance levels<sup>25</sup>. From kinetic considerations, we assessed that perovskite PVs should be capable of sustaining high efficiency under concentrated sunlight. This collectively makes perovskites very interesting for consideration in low-concentration-factor CPV applications.

Here, we experimentally assess a range of perovskite solar cells for both performance and stability under high-intensity irradiance. We fabricate CPV devices based on different perovskites as absorbers. The lead tri-(iodide-bromide) perovskites that we use are of the general form  $APbX_3$ , with the A-site cation being archetypal methylammonium (MA), mixed-cation formamidinium–caesium (FA/Cs), or triple-cation methylammonium–formamidinium–caesium (FA/MA/Cs). We compare their device performance under a wide range of monochromatic light intensities. Through spectroscopic and thermogravimetric analysis, we also investigate the intrinsic material stability. We observe that the FA/Cs perovskite composition delivers the most stable perovskite cells under high irradiance. We find that these perovskite solar cells can perform well on most performance parameters up to 53 times equivalent solar concentration, with a continuous linear increase in short-circuit current density ( $J_{sc}$ ) and a semi-logarithmic increase in open-circuit voltage ( $V_{oc}$ ). However, they lose fill factor (FF) for intensities beyond 10 Suns, which we identify to be primarily limited by the series resistance in the charge extraction layers. Importantly, we also demonstrate hundreds of hours of operational stability under 10 Suns irradiance. Our proof-of-principle study demonstrates that metal halide perovskites should be considered as a serious option for low-concentration factor CPVs and highlights areas for further focus of research activities.

## Material stability

We first investigate the fundamental stability under high irradiance of both thin films and devices comprising a range of different perovskite compositions, and present our results and associated discussion in Supplementary Notes 1–3 and Supplementary Figs. 1–6. From the materials assessed, we find that  $FA_{0.85}Cs_{0.17}Pb_{1.27}Br_{0.3}$  (FA/Cs) is the most stable composition, and FA/Cs devices deliver the highest efficiency under high irradiance. We therefore focus on this FA/Cs composition for our CPV study here.

## CPV performance under concentrated sunlight

We now inspect the CPV performance of the FA/Cs cell under simulated AM 1.5G full-spectrum sunlight. We show the spectrum of the concentrated light source in Supplementary Fig. 7 and the corresponding set-up in Supplementary Fig. 8. We give more details of our measurement and spectral mismatch estimation in the experimental section. In Fig. 2a, we show the  $J$ – $V$  curve of our highest-performing FA/Cs device measured under AM 1.5G  $100\text{ mW cm}^{-2}$  irradiance (1 Sun) with a two-wire connection under source mode. The device has a  $J_{sc}$  of  $23.2\text{ mA cm}^{-2}$ , a FF of 0.80 and a  $V_{oc}$  of 1.14 V, yielding a PCE of 21.1%. In Supplementary Fig. 9, we show the photovoltaic performance parameters extracted from  $J$ – $V$  curves (Fig. 2b) measured via four-wire source and sense mode, which overcomes resistive losses in the electrical cables, and contact resistance between the connecting pins. In Fig. 2c–f, we show the statistics of photovoltaic characteristics of the entire device population under various concentrations. We observe a linear increase in the  $J_{sc}$  and a semi-logarithmic increase in the  $V_{oc}$  with increasing light intensity. Notably, the  $V_{oc}$  reaches a substantial value of 1.26 V at a high concentration of 53 Suns. Though the  $V_{oc}$  increases at a rate of 80 mV per decade, the main limitation remains the FF, but this does not start to deteriorate significantly until intensities above 10 Suns. Nevertheless, we achieve an efficiency of 23.6% under 14 Suns and 22.9% under 31 Suns from a relatively stable FA/Cs perovskite solar cell.

Returning to the  $V_{oc}$ , we would expect the  $V_{oc}$  to increase monotonically with increasing charge-carrier density within the perovskite film and never reduce with increasing light intensity<sup>7,26</sup>. We have recently theoretically assessed the fundamental limitations of perovskite solar cells under high irradiance. Simply based on the spectroscopically derived recombination rates, and with assumptions about charge collection rates, we estimated that the  $V_{oc}$  should continuously rise and the efficiency should increase with irradiance, to over 100 Suns irradiance<sup>25</sup>. To verify that the perovskite absorber layer itself is not limiting the performance of our solar cells under high irradiance, we consider the recombination processes occurring with the FA/Cs perovskite absorber: we know that at low charge-carrier densities monomolecular processes dominate recombination. Under these conditions, charge recombination occurs through traps, or to a background of doped carriers, with characteristic recombination rate constant  $k_1$  and total recombination rate proportional to the charge density ( $n$ ). At intermediate charge densities, band-to-band bimolecular processes dominate recombination, with characteristic rate constant  $k_2$  and total rate proportional to  $n^2$ . Under high charge densities, third-order Auger process dominates recombination<sup>27</sup>, with a characteristic rate constant of  $k_3$  and the total rate proportional to  $n^3$ . With prior knowledge of these rate constants for the different perovskite absorber materials, which have been determined from spectroscopic studies, and by assuming steady-state conditions at open circuit, we can estimate the equivalent charge density, and the equivalent solar concentration factor ( $C$ ), at which the transition between these different regimes will occur. In addition, knowing the total recombination rate and the charge-carrier diffusion coefficient, we can estimate how the charge-carrier diffusion length within the absorber layer should change with charge density and solar concentration factor. In Fig. 3 we show the calculated charge-carrier diffusion length plotted against

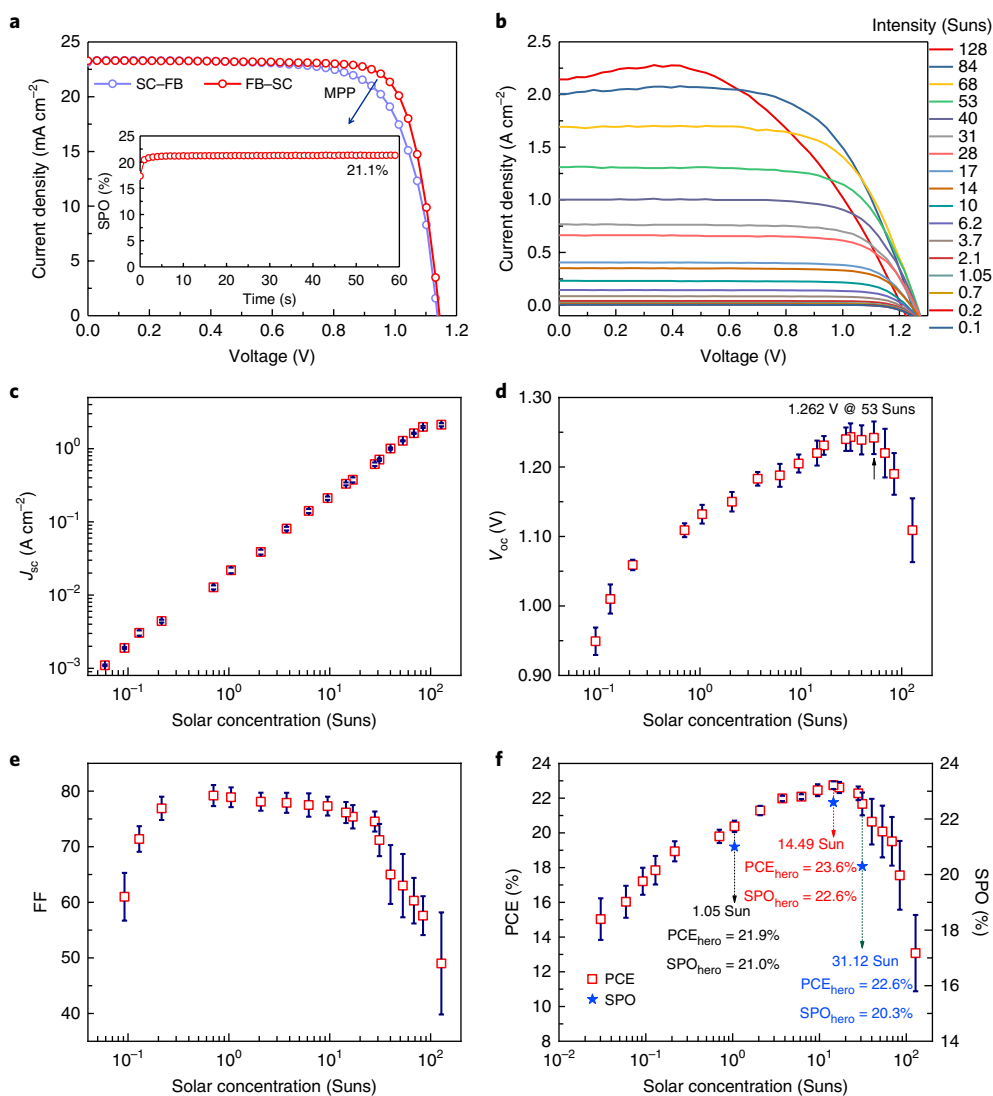


**Fig. 2 | CPV device performances.** **a**,  $J$ - $V$  characteristic of best-performing FA/Cs perovskite solar cell with an optically masked active area of  $\sim 9.19$  mm<sup>2</sup>, measured from forward bias (FB) to short-circuit (SC) and back again with a scan rate of  $380$  mV s<sup>-1</sup> under simulated AM 1.5 G solar irradiance at  $100$  mW cm<sup>-2</sup> (1 Sun) with two-wire connections under source mode. The inset shows the corresponding stabilized power output (SPO) data, determined by holding the cell at a fixed voltage near the maximum power point on the  $J$ - $V$  curve for  $60$  s. The cell structure is glass/FTO/SnO<sub>2</sub>/FA<sub>0.83</sub>Cs<sub>0.17</sub>PbI<sub>2.7</sub>Br<sub>0.3</sub>/spiro-OMeTAD/Au. **b**, Measured  $J$ - $V$  characteristics of the best-performing device under simulated concentrated AM 1.5 G sunlight at various irradiance levels. The active cell area was  $\sim 0.82$  mm<sup>2</sup> for the devices measured under high irradiance. The area was kept small to reduce parasitic series resistance losses. **c-f**, Comparison of  $J_{sc}$  (**c**),  $V_{oc}$  (**d**), FF (**e**) and PCE (**f**) of perovskite solar cell devices measured under various solar concentration factors (up to 128 Suns). Each average (symbol) and standard deviation (error bar) was calculated from eight devices. The PCE<sub>hero</sub> and SPO<sub>hero</sub> values represent the highest scanned efficiency and stabilized efficiency, respectively, measured from the best-performing device. The star symbols represent the SPO<sub>hero</sub> values. High-intensity illumination was with an AM 1.5 G filtered xenon lamp as solar simulator with a parabolic reflector and neutral density filters used to vary the irradiance levels (see spectrum in the Supplementary Fig. 7). All the light intensity measurements are performed on unsealed cells in ambient air under a four-wire, source and sense mode.

charge-carrier density, and we tabulate the equivalent solar concentration factors at the transition between the different dominating modes for charge recombination for the MA and FA/Cs perovskites. We give a full description of our estimations in Supplementary Note 4 and Supplementary Table 1.

As we show in Fig. 3, we determine that the recombination within the FA/Cs perovskite film should remain dominated by monomolecular processes up until around 230 Suns, and bimolecular recombination should then dominate until concentrations above 14,000 Suns, where Auger recombination starts to dominate. Additionally, for the FA/Cs perovskite, the charge-carrier diffusion length remains greater than  $4$   $\mu$ m until the concentration is over 100

Suns, and greater than  $1.5$   $\mu$ m until over 10,000 Suns. Therefore, by simply considering the metal halide perovskite absorber layer, we would expect the perovskite solar cells to operate efficiently up to concentrations well beyond 1,000 Suns.

Our estimates for diffusion length and carrier recombination processes are encouraging for the potential use of perovskite absorbers in CPV but imply that our observed 'saturation' and further reduction in  $V_{oc}$  with increasing light intensity must originate from other 'non-perovskite' components of the cells, or changes to the perovskite absorber with increasing light intensity, such as increased trap density (monomolecular recombination rate) or degradation. In our measurements, we start at low intensity and increase, and we

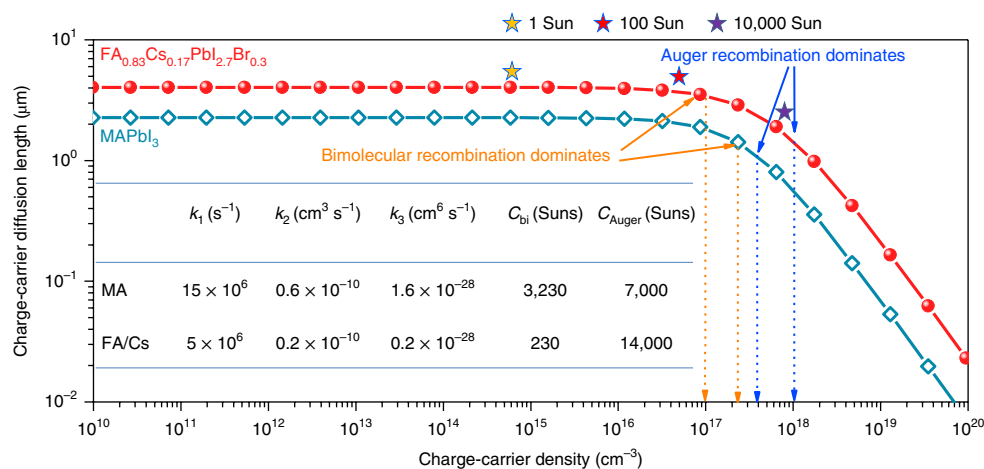


**Fig. 3 | Charge-carrier diffusion length and recombination processes.** Calculated charge-carrier diffusion lengths as a function of charge-carrier density. The inset table shows the estimated equivalent solar light concentration factors when recombination is dominated by bimolecular recombination ( $C_{bi}$ ) and Auger recombination ( $C_{Auger}$ ). MA and FA/Cs stand for MAPbI<sub>3</sub> and FA<sub>0.83</sub>CS<sub>0.17</sub>PbI<sub>2.7</sub>Br<sub>0.3</sub>, respectively. The monomolecular recombination rate constant ( $k_1$ ), bimolecular recombination rate constant ( $k_2$ ) and Auger recombination rate constant ( $k_3$ ) of the MA absorber layers are extracted from ref.<sup>38</sup> and those for the FA/Cs absorber layers from ref.<sup>39</sup>. The star symbols represent the estimated equivalent solar concentration required to generate the corresponding charge-carrier density for the FA/Cs perovskite.

observe that the measurement of  $V_{oc}$  versus Suns at high irradiance is not reversible. We show a repetitive measurement of a cell under 142 Suns in Supplementary Fig. 10, where we observe a progressive drop in  $J_{sc}$  and  $V_{oc}$ . Therefore, under the highest-intensity light exposure in air, we are inducing permanent degradation of the cells. We thus consider this intensity at peak  $V_{oc}$  to indicate a degree of photo-stability of the perovskite film and device in ambient conditions, rather than a fundamental limitation of electronic properties.

Traditionally, information about the ‘mode’ of recombination can be gained by estimating the ‘ideality factor’ of the solar cell. This is how closely the operational characteristics of the solar cell represent those expected from an electronic model of a single diode. A numerical factor—the ideality factor—is inserted in the diode equation, as we describe in Supplementary Note 5. This factor can carry some physical meaning, where an ideality factor of 1 traditionally implies that all recombination is bimolecular, and an ideality factor of 2 implies that all recombination is monomolecular and is proceeding via trap-assisted recombination<sup>28</sup>. According to our estimations above, we expect to be in the monomolecular regime over these intensity ranges and hence expect the ideality factor to be approximately 2. However, from the slope of the  $V_{oc}$  versus light intensity, we estimate an ideality factor of 1.3. We also estimate the ideality factor from fitting of the  $J$ - $V$  curves, which we show in Supplementary Fig. 11. This figure shows a variable ideality factor which increases from less than 1 at low concentrations to 4.5 at the highest concentrations. Ideality factors of greater than 2 have a non-physical meaning according to traditional theory. These apparently non-physical and variable ideality factors are likely to originate from the combined presence of both mobile ions and traps in the perovskite semiconductors, part of the same mechanism that results in hysteresis in the  $J$ - $V$  curves of the perovskite solar cells<sup>29,30</sup>. Under different electrical bias and light exposure regimes, ions will migrate to different regions of the solar cells and either make the conditions favourable to stabilize filled traps near the surface of the perovskite absorber layer or make the conditions favourable to induce rapid depopulation of traps. When the traps are mostly filled, we expect to have a smaller fraction of trap-assisted recombination, longer charge diffusion lengths and an ideality factor closer to 1. When the traps are predominantly empty, we expect to have a higher fraction of trap-assisted recombination, shorter diffusion lengths and a higher ideality factor. Recently, Barnes and co-workers highlighted

the challenges with ideality factor estimations, and suggest measuring the transient  $V_{oc}$  as a function of light intensity as a means to derive the ideality factor<sup>31</sup>. Tress et al. also estimated variable ideality factors for perovskite solar cells and advocate fitting of dark  $J$ - $V$  measurements as a suitable methodology<sup>32</sup>. This aspect requires further investigation.

As discussed above, we do not expect limitations on charge extraction from the perovskite layer to set in until solar concentrations beyond 1,000 Suns. Therefore, this ‘FF roll-off’ is likely to originate from resistance from the charge extraction layers, contact resistance between the internal layers of the solar cell, or simply parasitic resistance in the fluorine-doped tin oxide (FTO) transparent conducting electrodes, as has been previously observed for organic photovoltaics<sup>33,34</sup>. To disentangle the contributions to series resistance in our cells, we have performed measurements on the individual components, by measuring  $J$ - $V$  curves of ‘sub-cells’, which have the same architecture as the solar cells but with many layers, including the perovskite absorber layer, missing. In the same manner as for the solar cells, for all the sub-cells we include an additional electrically conductive silver ribbon adhesive to minimize the series resistance for the charge conducted through the FTO to the gold metallic contact. The sub-cells are FTO/Au to estimate the series resistance in the FTO and metallic conductors; FTO/SnO<sub>2</sub>/Au to estimate the additional series resistance contribution from the n-type charge collection layer; and FTO/spiro-OMeTAD/Au to estimate the series resistance contribution from the hole-conductor. We show the results in Supplementary Fig. 12 and Supplementary Table 2. We find that the main resistance originates from the spiro-OMeTAD layer, and the combined contribution from the FTO, SnO<sub>2</sub> and spiro-OMeTAD add up to closely match the series resistance of the solar cell, as determined by the slope of the  $J$ - $V$  curve at  $V_{oc}$ . Therefore, to improve the efficiency of our perovskite CPV devices further under higher irradiance levels, we need to find charge extraction layers that have much lower series resistance than spiro-OMeTAD and SnO<sub>2</sub>, and use higher conductivity TCOs or metallic grids for charge extraction.

We note that we did not actively cool the devices during the increasing irradiance tests. We estimate the cell temperature during operation with an infrared camera, as we show in Supplementary Fig. 13, and measure the cell surface temperature to rise from 23°C to 38°C, over the course of a typical measurement. This

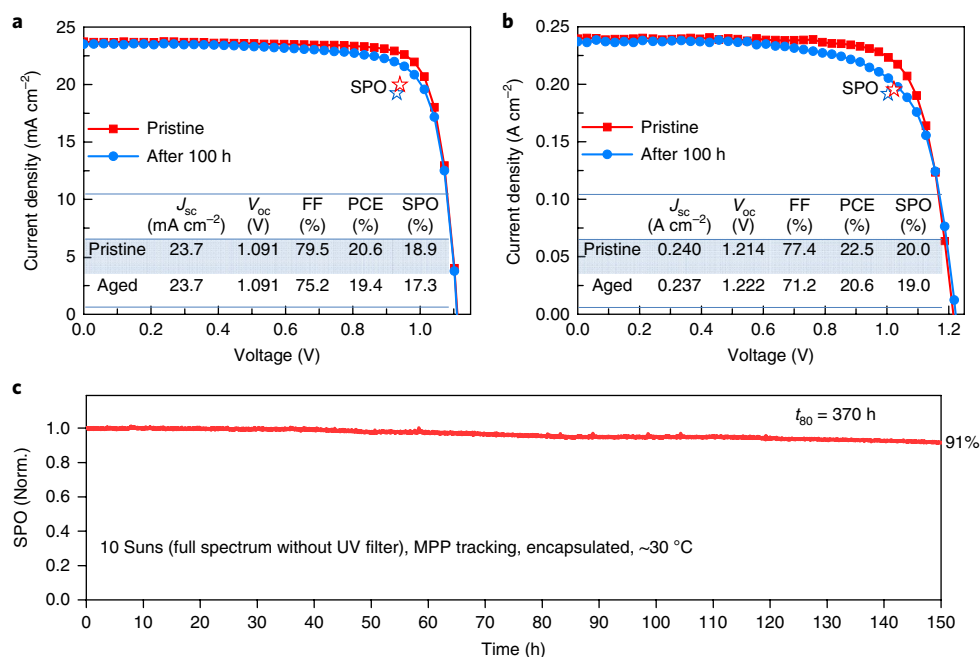


**Fig. 4 | CPV stability under concentrated light. a,b**,  $J$ - $V$  curves of the pristine and aged devices measured under 1 Sun (**a**) and 10 Sun irradiance (**b**). The insets give the  $J$ - $V$  curve performance parameters and the large star symbols show the SPO values. **c**, SPO of the perovskite devices, continuously recorded under 10 Sun concentration. The  $t_{80}$  lifetime represents the time it takes for the SPO to reduce to 80% of its initial value. The device structure is FTO/SnO<sub>2</sub>/PCBM/FA<sub>0.83</sub>Cs<sub>0.17</sub>PbI<sub>2.7</sub>Br<sub>0.3</sub>/PTAA/Au. Illumination was with a xenon lamp full-spectrum AM 1.5 G simulator (spectrum shown in Supplementary Fig. 18). The device is held at maximum power point during aging and kept at a constant temperature by an air stream flowing onto the devices (FTO side), with the device surface measuring approximately 30 °C. All measurements were performed on encapsulated cells in ambient air. The active cell area was ~0.87 mm<sup>2</sup>, to reduce parasitic series resistance losses.

increase in cell temperature will also contribute to the lower than expected  $V_{oc}$  at high irradiance levels, since  $V_{oc}$  drops with increasing temperature<sup>35,36</sup>. The stability of this perovskite CPV device from prolonged exposure to high irradiance levels is poor, as we show in Supplementary Fig. 14, which we postulate to be limited by the instability introduced by using the spiro-OMeTAD hole-transporting layer. To tackle this instability, we optimize cells using poly[bis(4-phenyl)(2,5,6-trimethylphenyl)amine] (PTAA) as the hole-transporting layer. Furthermore, we coat the SnO<sub>2</sub> compact layer with a thin layer of 4-(1,3-dimethyl-2,3-dihydro-1H-benzimidazol-2-yl)-*N,N*-diphenylaniline (*N*-DPBI)-doped phenyl-C<sub>61</sub>-butyric acid methyl ester (PC<sub>61</sub>BM) to further enhance the device stability<sup>23</sup>. These ‘improved stability’ devices have a structure of glass/FTO/SnO<sub>2</sub>/PC<sub>61</sub>BM/perovskite/PTAA/Au, which delivers similar efficiency to those devices using spiro-OMeTAD under 1 Sun and higher irradiance, which we show in Supplementary Figs. 15, 16 and 17.

To assess the stability of these devices under high irradiance, we measure the stabilized efficiency of the encapsulated solar cells glass/FTO/SnO<sub>2</sub>/PC<sub>61</sub>BM/perovskite (FA/Cs)/PTAA/Au solar cells by holding them at the maximum power point under concentrated sunlight (10 Sun) and present the results in Fig. 4. We actively cool the cell with flowing air from a compressed air source, maintaining the cell temperature at ~30 °C. Encouragingly, we observe excellent stability under 10 Sun irradiance, with the cell maintaining 91% of its original efficiency after 150 h. From the  $J$ - $V$  curves measured during the aging process (Fig. 4a,b), we determine that the degradation is mainly due to the drop in FF. We determine the lifetime to 80% degradation ( $t_{80}$ ) at 10 Sun irradiance to be 370 h.

## Conclusion

We have experimentally demonstrated increased efficiency and substantial stability of perovskite solar cells under simulated

concentrated solar irradiance. By comparing the structural, optical and optoelectronic properties of MA, FA/MA/Cs and FA/Cs perovskite films, we identify the FA/Cs perovskite as the most suitable, owing to improved thermal stability and higher tolerance to high levels of irradiance. By using the FA/Cs perovskite as a photoactive layer in a single-junction solar cell, we boost the PCE from 21.1% under 1 Sun, to 23.6% under 14 Sun irradiance. We have found that the key limiting factor with increasing irradiance is a deterioration of the FF at concentrations above 10 Sun, which should be surmountable by future adaptations to reduce the series resistance contribution from the charge extraction layers. We note that the  $V_{oc}$  of our best-performing FA/Cs device reaches 1.26 V at 53 Sun concentration, indicating the potential of perovskite solar cells for CPV applications. Of critical importance, the FA/Cs device using relatively stable interfacial layers sustains over 90% of its original efficiency after 150 h aging at 10 Sun concentrated sunlight. We expect the material innovation and fast developments in the perovskite field of research to enable efficient and stable perovskite CPVs to be realized in the near future, ultimately using perovskite tandem and triple-junction cells for maximum power conversion efficiency. Beyond strategies to further increase the efficiency, there are four key areas that we believe require scrutiny and enhancement. First, the series resistance in the charge extraction layers needs to be reduced, to improve FF under high irradiance levels. Second, we need better understanding of the present limitations and improvements to the long-term operational stability under high levels of irradiance and elevated temperatures. Third, the cell design and thermal management strategies need to be adapted to enable the cells to operate at as low a temperature as possible under concentrated sunlight. Finally, strategies should be developed for the optical design of the concentrating optics, including macroscopic lenses, parabolic mirrors and micro-lenses, to achieve an economically viable, deployable perovskite CPV technology under low-concentrated sunlight.

## Methods

**Preparation of perovskite films.** MAPbI<sub>3</sub> solution: 1.2 M perovskite precursor solution was prepared using a 4:1 (v:v) mixed solvent from anhydrous DMF and DMSO (Sigma-Aldrich), with the desired composition obtained by using precursor salts: methylammonium iodide (MAI; Dyesol), lead iodide (PbI<sub>2</sub>; TCI). FA<sub>0.83</sub>Cs<sub>0.17</sub>PbI<sub>2.7</sub>Br<sub>0.3</sub> solution: 1.45 M perovskite precursor solution was prepared using a 4:1 (v:v) mixed solvent from anhydrous DMF and DMSO (Sigma-Aldrich), with desired composition obtained by using precursor salts: formamidinium iodide (FAI; Dyesol), caesium iodide (CsI; Alfa Aesar), PbI<sub>2</sub> (TCI), lead bromide (PbBr<sub>2</sub>; TCI). FA<sub>0.79</sub>MA<sub>0.16</sub>Cs<sub>0.05</sub>PbI<sub>2.7</sub>Br<sub>0.3</sub> solution: 1.45 M perovskite precursor solution was prepared using a 4:1 (v:v) mixed solvent from anhydrous DMF and DMSO (Sigma-Aldrich), with desired composition obtained by using precursor salts: FAI (Dyesol), MAI (Dyesol), CsI (Alfa Aesar), PbI<sub>2</sub> (TCI), PbBr<sub>2</sub> (TCI). All solutions were prepared in a nitrogen-filled glovebox and kept stirring overnight at room temperature. The MAPbI<sub>3</sub> films were deposited through a two-step spin-coating programme (10 s at 1,000 r.p.m. and 15 s at 5,000 r.p.m.) with dripping of anisole (Sigma-Aldrich) as anti-solvent during the second step, 10 s before the end. The films were then transferred to a hotplate immediately and annealed at 100 °C for 10 min. For the FA/Cs and FA/MA/Cs perovskite films, the precursor solutions were spin-coated through a two-step spin-coating programme (10 s at 1,000 r.p.m. and 35 s at 6,000 r.p.m.) with dripping of anisole (Sigma-Aldrich) as anti-solvent during the second step, 10 s before the end. The films were then annealed at 100 °C for 60 min. All films were spin-coated in a dry box with relative humidity below 20%.

**X-ray diffraction.** All X-ray diffraction spectra were obtained on a Rigaku SmartLab X-ray diffractometer with CuK<sub>α1</sub> (1.54060 Å) and a HyPix-3000 2D hybrid pixel array detector, and operated at 40 kV with a 2θ scan range of 10–30°.

**Thermogravimetric analysis.** We first deposited perovskite films on glass substrates using the same procedure for device fabrication. Then we scratched the well-crystallized perovskite films from the glass substrate and collected the perovskite powders for thermogravimetric measurement. Thermogravimetry was carried out in open ceramic pans under a constant flow of nitrogen at 200 ml min<sup>-1</sup> using a Perkin Elmer thermogravimetry/differential thermal analyser (TG/DTA). Each sample was heated from room temperature to 800 °C under nitrogen using a scan rate of 10 °C min<sup>-1</sup>.

**Photoluminescence measurement.** The photoluminescence spectra were collected with an intensified charge-coupled device (iCCD, PI-MAX4, Princeton Instruments), photoexcited by a 400 nm laser operated in continuous-wave mode with a fluence of ~790 mW cm<sup>-2</sup> calibrated with a power meter, which generates equivalent carrier density with 10 Suns irradiance of white light. More details about the conversion of equivalent power are described in Supplementary Note 3.

**Fabrication of perovskite solar cell devices.** For the electron-transporting layer, 0.05 M SnCl<sub>4</sub>·5H<sub>2</sub>O (Sigma-Aldrich) was first dissolved in anhydrous isopropanol and stirred for 30 min at room temperature. The solution was deposited on cleaned FTO substrates with 3,000 r.p.m. spin rate for 30 s, followed by pre-drying at 100 °C for 10 min, and then heat-treated at 180 °C for 1 h. The films were then treated using chemical bath deposition method, as described elsewhere<sup>37</sup>. Urea (500 mg, Sigma-Aldrich) was dissolved in 40 ml deionized water, followed by the addition of 10 ml 3-mercaptopropionic acid (Sigma-Aldrich) and 0.5 ml HCl (37 wt%). Finally, SnCl<sub>4</sub>·2H<sub>2</sub>O (Sigma-Aldrich) was dissolved in the solution at 0.002 M and stirred for 2 min. The deposition was made by putting the substrates in a glass petri dish filled with the above solution in a 70 °C oven for 3 h. The treated substrates were rinsed in a sonication bath of deionized water for 2 min, dried in a stream of nitrogen and annealed for 1 h at 180 °C. For the stability test, we further add a layer of doped PC<sub>61</sub>BM: we dissolve PC<sub>61</sub>BM (Solenne) in anhydrous 1,2-dichlorobenzene (DCB; Sigma-Aldrich) at 10 mg ml<sup>-1</sup>. We dissolve the dopant 4-(1,3-dimethyl-2,3-dihydro-1H-benzimidazol-2-yl)-N,N-diphenylaniline (N-DPBI; Sigma-Aldrich) dissolved in DCB at 10 mg ml<sup>-1</sup>. Both of the PCBM and N-DPBI solutions were stirred overnight at room temperature. Before deposition, we add 20 μl of N-DPBI solution in 1 ml PCBM precursor solution. Then we spin-coat the doped PCBM solution on top of the as-prepared SnO<sub>2</sub> layer in a nitrogen-filled glovebox at 4,000 r.p.m. for 40 s and anneal in nitrogen at 80 °C overnight to achieve successful doping. More details are reported elsewhere<sup>23</sup>.

For the perovskite absorber layer, we use the same protocols as for the thin film fabrication.

For the 2,20,7,70-tetrakis[N,N-di(4-methoxyphenyl)amino]-9,90-spirobifluorene (spiro-OMeTAD) hole-transporting layer, to obtain a spiro-OMeTAD solution, we dissolved 85.7 mg spiro-OMeTAD (Boron Technology) in 1 ml anhydrous chlorobenzene with additives of 28.8 μl tert-butylpyridine (tBP) and 20 μl lithium bis(trifluoromethylsulfonyl)imide (Li-TFSI) salt in acetonitrile (520 mg ml<sup>-1</sup>). For the PTAA hole-transporting layer, to obtain a PTAA solution, we dissolved 10 mg PTAA (Flexink) in 1 ml anhydrous chlorobenzene. Tris(pentafluorophenyl)borane (Sigma-Aldrich) was dissolved in anhydrous chlorobenzene and mixed with PTAA at a ratio of 20 mol%. After the perovskite films cooled to room temperature, the spiro-OMeTAD was spin-coated on the perovskite layer at 2,500 r.p.m. for 40 s in a dry box (relative humidity <20%) as

a hole-transporting layer. When using the PTAA as a hole-transporting layer, we further spin-coat a tBP solution (33 μl of tBP in 1 ml of chlorobenzene) on perovskite films at 4,000 r.p.m. for 30 s and annealed at 100 °C for 10 min, prior to the PTAA deposition. Then, the PTAA solution was spin-coated at 2,500 r.p.m. for 40 s in a dry box (relative humidity <20%).

For the electrode deposition, 100 nm gold electrodes were thermally evaporated under vacuum of ~5 × 10<sup>-6</sup> Torr, at a rate of ~1 Å s<sup>-1</sup>. Note that the temperature of the vacuum chamber was controlled at under 35 °C during the evaporation of metal electrode; a higher temperature will cause possible degradation of perovskite films.

**Current–voltage measurements under AM 1.5 G sunlight.** The *J*–*V* curves were measured (2400 Series SourceMeter, Keithley Instruments) under simulated AM 1.5 G sunlight at 100 mW cm<sup>-2</sup> irradiance generated by an Abet Class AAB Sun 2000 simulator, with the intensity calibrated with a KG3 filtered Si reference cell calibrated by the National Renewable Energy Laboratory. The mismatch factor was calculated to be less than 2% and applied to calibrate the AM 1.5 G 100 mW cm<sup>-2</sup> equivalent irradiance. The active area of the solar cell measured under AM 1.5 G is 9.19 mm<sup>2</sup>, defined by an opaque aperture mask. For the cells measured under simulated concentrated sunlight, the cell area was mechanically scribed down to ~1 mm<sup>2</sup> to reduce series resistance in the FTO. To determine the active area of the small cell, we measured the unmasked small cells under AM 1.5 G illumination and matched the *J*<sub>sc</sub> measured with the same cell before scribing, measured through the 9.19 mm<sup>2</sup> aperture mask, as illustrated in Supplementary Fig. 3. This enabled us to measure the small-area cells unmasked, without inducing significant errors from estimations of small masking areas and from shading losses that are difficult to quantify. The *J*–*V* scans were measured from forward bias to short-circuit at a scan rate of 380 mV s<sup>-1</sup>. A stabilization time of 5 s at forward bias of 1.4 V under illumination was done before scanning.

**Current–voltage measurements under concentrated sunlight.** To avoid the effect of parasitic resistance, the active area of the perovskite solar cells was reduced to ~1 mm<sup>2</sup>. The concentrated light source was obtained by focusing a xenon lamp simulated white-light source including an AM 1.5 G filter. The light intensity was modulated by a set of neutral density filters, and the irradiance was determined using a KG3 filtered silicon reference cell and accounting for spectral mismatch, as described in the Supplementary Note 6 and Supplementary Fig. 18. To set the '1 Sun intensity', the perovskite test cell was used for self-calibration between the AAB class simulator and the concentrated solar simulator. To quantify the intensity on the concentrated solar simulator, at near 1 Sun intensity, the *J*<sub>sc</sub> was measured on the test cell and compared to the *J*<sub>sc</sub> measured on the same cell, under the mismatch factor corrected AAB class AM 1.5 G 100 mW cm<sup>-2</sup> solar simulator. The *J*–*V* curves were recorded with a 2400 Series source meter (Keithley Instruments) via a four-wire connection mode, which overcomes resistive losses in the electrical cables, and contact resistance between the connecting pins.

**External quantum efficiency measurement.** External quantum efficiency was evaluated via custom-built Fourier transform photocurrent spectroscopy based on the Bruker Vertex 80 v Fourier transform spectrometer. A Newport AAA Sun simulator was used as the light source, and the light intensity was calibrated with a Newport-calibrated reference silicon photodiode.

**Stability test.** For stability measurement, the perovskite devices were encapsulated with ultraviolet adhesive (LT-U001, Lumtec) and a glass coverslip as a barrier layer in a nitrogen-filled glovebox. Before encapsulation, we blew the devices with a nitrogen gun to remove contamination and stored them in a nitrogen-filled glovebox for overnight to remove any residual moisture. The devices were aged at maximum power point under concentrated full spectrum simulated AM 1.5 G, 100 mW cm<sup>-2</sup> irradiance. The device was constantly cooled by blasting compressed air stream onto the devices (FTO side) with the device surface measuring approximately 30 °C. We do not have control of the humidity but monitored the laboratory humidity, which ranged from 40% to 50% relative humidity at room temperature, during the course of the aging.

**Data Availability.** The data that support the plots within this paper and other findings of this study are available from the corresponding author upon reasonable request.

Received: 30 November 2017; Accepted: 5 July 2018;  
Published online: 6 August 2018

## References

- More than half of utility-scale solar photovoltaic systems track the sun through the day (US EIA, 2017); <https://www.eia.gov/todayinenergy/detail.php?id=30912>
- Wiesenfarth, M., Philipps, S. P., Bett, A. W., Horowitz, K. & Kurtz, S. *Current Status of Concentrator Photovoltaic (CPV) Technology* (National Renewable Energy Laboratory, 2017).

3. Apostoleris, H., Stefanchik, M. & Chiesa, M. Tracking-integrated systems for concentrating photovoltaics. *Nat. Energy* **1**, 16018 (2016).
4. Dahal, R., Li, J., Aryal, K., Lin, J. Y. & Jiang, H. X. InGaN/GaN multiple quantum well concentrator solar cells. *Appl. Phys. Lett.* **97**, 073115 (2010).
5. Cotal, H. et al. III–V multijunction solar cells for concentrating photovoltaics. *Energy Environ. Sci.* **2**, 174–192 (2009).
6. Green, M. A. et al. Solar cell efficiency tables (version 50). *Prog. Photovolt. Res. Appl.* **25**, 668–676 (2017).
7. Tress, W. Perovskite solar cells on the way to their radiative efficiency limit — insights into a success story of high open-circuit voltage and low recombination. *Adv. Energy Mater.* **7**, 1602358 (2017).
8. Varieras, R. V., Wang, J. & King, D. L. System performance considerations for low-concentration linear-focus silicon-based photovoltaic modules. *IEEE J. Photovolt.* **3**, 1409–1414 (2013).
9. Kojima, A., Teshima, K., Shirai, Y. & Miyasaka, T. Organometal halide perovskites as visible-light sensitizers for photovoltaic cells. *J. Am. Chem. Soc.* **131**, 6050–6051 (2009).
10. Lee, M. M., Teuscher, J., Miyasaka, T., Murakami, T. N. & Snaith, H. J. Efficient hybrid solar cells based on meso-superstructured organometal halide perovskites. *Science* **338**, 643–7 (2012).
11. Kim, H.-S. et al. Lead iodide perovskite sensitized all-solid-state submicron thin film mesoscopic solar cell with efficiency exceeding 9%. *Sci. Rep.* **2**, 591 (2012).
12. NREL efficiency chart. Available at [http://www.nrel.gov/ncpv/images/efficiency\\_chart.jpg](http://www.nrel.gov/ncpv/images/efficiency_chart.jpg) (accessed 16 June 2018).
13. Yang, W. S. et al. Iodide management in formamidinium-lead-halide-based perovskite layers for efficient solar cells. *Science* **356**, 1376–1379 (2017).
14. Bush, K. A. et al. 23.6%-efficient monolithic perovskite/silicon tandem solar cells with improved stability. *Nat. Energy* **2**, 17009 (2017).
15. Duong, T. et al. Rubidium multication perovskite with optimized bandgap for perovskite-silicon tandem with over 26% efficiency. *Adv. Energy Mater.* **7**, 1700228 (2017).
16. Hörantner, M. T. et al. The potential of multijunction perovskite solar cells. *ACS Energy Lett.* **2**, 2506–2513 (2017).
17. Zhou, Y. & Gray-Weale, A. A numerical model for charge transport and energy conversion of perovskite solar cells. *Phys. Chem. Chem. Phys.* **18**, 4476–4486 (2015).
18. Adhikari, K. R., Gurung, S., Bhattarai, B. K. & Mari, B. Dependence of perovskite solar cells performance on temperature and solar irradiation. In *3rd Int. Renew. Sustain. Energy Conf.* 1–6 (2015); <https://doi.org/10.1109/IRSEC.2015.7455146>
19. Leong, W. L. et al. Identifying fundamental limitations in halide perovskite solar cells. *Adv. Mater.* **28**, 2439–2445 (2016).
20. Law, C. et al. Performance and stability of lead perovskite/TiO<sub>2</sub>, polymer/PCBM, and dye sensitized solar cells at light intensities up to 70 suns. *Adv. Mater.* **26**, 6268–6273 (2014).
21. Leijtens, T. et al. Overcoming ultraviolet light instability of sensitized TiO<sub>2</sub> with meso-superstructured organometal tri-halide perovskite solar cells. *Nat. Commun.* **4**, 2885 (2013).
22. Conings, B. et al. Intrinsic thermal instability of methylammonium lead trihalide perovskite. *Adv. Energy Mater.* **5**, 1500477 (2015).
23. Wang, Z. et al. Efficient and air-stable mixed-cation lead mixed-halide perovskite solar cells with n-doped organic electron extraction layers. *Adv. Mater.* **29**, 1604186 (2017).
24. Wang, Z. et al. Efficient and ambient-air-stable solar cells with 2D–3D hetero-structured butylammonium–caesium–formamidinium lead halide perovskites. *Nat. Energy* **2**, 17135 (2017).
25. Lin, Q., Wang, Z., Snaith, H. J., Johnston, M. B. & Herz, L. M. Hybrid perovskites: prospects for concentrator solar cells. *Adv. Sci.* **5**, 1700792 (2018).
26. Saygili, Y. et al. Planar perovskite solar cells with high open-circuit voltage containing a supramolecular iron complex as hole transport material dopant. *ChemPhysChem* **19**, 1–9 (2018).
27. Herz, L. M. Charge-carrier mobilities in metal halide perovskites: fundamental mechanisms and limits. *ACS Energy Lett.* **2**, 1539–1548 (2017).
28. Lee, G. W., Shim, J. I. & Shin, D. S. On the ideality factor of the radiative recombination current in semiconductor light-emitting diodes. *Appl. Phys. Lett.* **109**, 031104 (2016).
29. Van Reenen, S., Kemerink, M. & Snaith, H. J. Modeling anomalous hysteresis in perovskite solar cells. *J. Phys. Chem. Lett.* **6**, 3808–3814 (2015).
30. Calado, P. et al. Evidence for ion migration in hybrid perovskite solar cells with minimal hysteresis. *Nat. Commun.* **7**, 13831 (2016).
31. Calado, P. et al. Identifying dominant recombination mechanisms in perovskite solar cells by measuring the transient ideality factor. Preprint at <https://arxiv.org/abs/1804.09049> (2018).
32. Tress, W. et al. Interpretation and evolution of open-circuit voltage, recombination, ideality factor and subgap defect states during reversible light-soaking and irreversible degradation of perovskite solar cells. *Energy Environ. Sci.* **11**, 151–165 (2018).
33. Manor, A., Katz, E. A., Tromholt, T., Hirsh, B. & Krebs, F. Origin of size effect on efficiency of organic photovoltaics. *J. Appl. Phys.* **109**, 074508 (2011).
34. Tromholt, T., Katz, E. A., Hirsch, B., Vossler, A. & Krebs, F. Effects of concentrated sunlight on organic photovoltaics. *Appl. Phys. Lett.* **96**, 075301 (2010).
35. Han, X., Qu, J. & Guo, Y. Dependence of silicon concentrator solar cells parameters on temperature and light intensity. *Taiyangneng Xuebao Acta Energ. Sol. Sin.* **36**, 1585–1590 (2015).
36. Hörantner, M. T. & Snaith, H. Predicting and optimising the energy yield of perovskite-on-silicon tandem solar cells under real world conditions. *Energy Environ. Sci.* **10**, 1983–1993 (2017).
37. Anaraki, E. H. et al. Highly efficient and stable planar perovskite solar cells by solution-processed tin oxide. *Energy Environ. Sci.* **9**, 3128–3134 (2016).
38. Milot, R. L., Eperon, G. E., Snaith, H. J., Johnston, M. B. & Herz, L. M. Temperature-dependent charge-carrier dynamics in CH<sub>3</sub>NH<sub>3</sub>PbI<sub>3</sub> perovskite thin films. *Adv. Funct. Mater.* **25**, 6218–6227 (2015).
39. Rehman, W. et al. Photovoltaic mixed-cation lead mixed-halide perovskites: links between crystallinity, photo-stability and electronic properties. *Energy Environ. Sci.* **10**, 361–369 (2017).

## Acknowledgements

This project has received funding from the European Union's Horizon 2020 research and innovation programme under both grant agreement no. 763977 of the PerTPV project and grant agreement no. 675867 of the INFORM project, and AFOSR through project FA9550-15-1-0115. B.W. acknowledges the European Commission for Marie Skłodowska-Curie actions individual fellowship (REA grant no. 706552-APPEL). We also thank R. Warren and R. Xiang for helping with light intensity measurements and illustrations.

## Author contributions

Z.W., Q.L. and H.J.S. conceived of the project. Z.W. designed the experiments and fabricated the devices and thin film samples. Z.W. performed the thermogravimetric and X-ray diffraction measurements and analysed the data. Q.L. carried out photoluminescence and external quantum efficiency measurements. Z.W. and Q.L. performed light intensity measurements. B.W. and M.G.C. helped with light intensity and four-wire measurements. Y.-H.L. contributed to hole-transporting layer deposition. M.T.K. performed spectral mismatch corrections. L.M.H. and M.B.J. supervised the optical spectroscopy experiments. H.J.S. supervised the whole project. Z.W. wrote the first draft of the paper. All authors discussed the results and contributed to the writing of the paper.

## Competing interests

H.J.S. is a co-founder and CSO of Oxford PV Ltd, a company that is commercializing perovskite PV technologies. All other authors declare no competing interests.

## Additional information

**Supplementary information** is available for this paper at <https://doi.org/10.1038/s41560-018-0220-2>.

**Reprints and permissions information** is available at [www.nature.com/reprints](http://www.nature.com/reprints).

**Correspondence and requests for materials** should be addressed to H.J.S.

**Publisher's note:** Springer Nature remains neutral with regard to jurisdictional claims in published maps and institutional affiliations.

## Solar Cells Reporting Summary

Nature Research wishes to improve the reproducibility of the work that we publish. This form is intended for publication with all accepted papers reporting the characterization of photovoltaic devices and provides structure for consistency and transparency in reporting. Some list items might not apply to an individual manuscript, but all fields must be completed for clarity.

For further information on Nature Research policies, including our [data availability policy](#), see [Authors & Referees](#).

### ► Experimental design

#### Please check: are the following details reported in the manuscript?

##### 1. Dimensions

- Area of the tested solar cells  Yes  No The active area of the standard size solar cell is 9.19 mm<sup>2</sup>. For concentrator photovoltaic (CPV) tests, the active area is reduced to ~1 mm<sup>2</sup>. Details are given in the method section.
- Method used to determine the device area  Yes  No For the standard-area devices, we employed an opaque mask of 0.0919 cm<sup>2</sup> metal aperture to define the active area and to eliminate edge effects. The electronic active area of the cell, as defined by the overlap of the FTO electrode and metal electrode, was ~ 0.12cm<sup>2</sup>. For the small-area CPV devices, no mask/aperture was used since the error of shadowing and area estimation of the small area masks are very high. Instead, as we clearly describe in the manuscript, we used the J<sub>sc</sub> measured on the properly masked and mismatch corrected standard area cell to "self-calibrate" the J<sub>sc</sub> and equivalent active area on the small area cell. A full description is given in the method section and Supplementary Information.

##### 2. Current-voltage characterization

- Current density-voltage (J-V) plots in both forward and backward direction  Yes  No We show the J-V plots from scans in both forward and backward directions.
- Voltage scan conditions  Yes  No We scan at a rate of 380 mV s<sup>-1</sup>.  
*For instance: scan direction, speed, dwell times*
- Test environment  Yes  No The measurements were carried out in air at room temperature.  
*For instance: characterization temperature, in air or in glove box*
- Protocol for preconditioning of the device before its characterization  Yes  No For the standard-area devices, a stabilisation time of 5 s at forward bias of 1.4 V under illumination was done prior to scanning. For the small-area devices measured under high irradiance, no preconditioning was applied.
- Stability of the J-V characteristic  Yes  No We show stabilized power output (SPO) data, determined by holding the cell at a fixed voltage near the maximum power point (MPP) on the J-V curve for 60 s.  
*Verified with time evolution of the maximum power point or with the photocurrent at maximum power point; see ref. 7 for details.*

##### 3. Hysteresis or any other unusual behaviour

- Description of the unusual behaviour observed during the characterization  Yes  No We discuss the stabilized power output in the text where we present the device performance.
- Related experimental data  Yes  No We show the reverse scanned JV curves and the stabilized power output.

##### 4. Efficiency

- External quantum efficiency (EQE) or incident photons to current efficiency (IPCE)  Yes  No We provided the EQE data under the standard reference spectrum which is comparable with the simulator. The EQE spectra were evaluated via custom-build Fourier transform photocurrent spectroscopy based on the Bruker Vertex 80v Fourier transform spectrometer. A Newport AAA sun simulator was used as light source and the light intensity was calibrated with a Newport-calibrated reference silicon photodiode. We show details in the method section and the supplementary information.

A comparison between the integrated response under the standard reference spectrum and the response measure under the simulator

Yes  
 No

The difference between the integrated current from EQE and the short-circuit current from the JV curve measured under AM 1.5G solar simulator is within 5% difference which is within the accuracy confidence of the measurements. We give full details in the method section and the Supplementary Fig. 18.

For tandem solar cells, the bias illumination and bias voltage used for each subcell

Yes  
 No

*State where this information can be found in the text.*

*Explain why this information is not reported/not relevant.*

## 5. Calibration

Light source and reference cell or sensor used for the characterization

Yes  
 No

The J-V curves are measured (2400 Series SourceMeter, Keithley Instruments) under simulated AM 1.5 sunlight at 100 mW cm<sup>-2</sup> irradiance generated by an Abet Class AAB sun 2000 simulator. For one set of concentrator PV measurements (presented in the Supplementary Information) we employed a monochromatic illumination source and fully describe the intensity calibration in the text. For the concentrator PV measurements in the main text, they were measured under xenon lamp based AM 1.5G simulator. We give full details about the calibration and mismatch factor estimations in the method section and Supplementary Notes.

Confirmation that the reference cell was calibrated and certified

Yes  
 No

The intensity was calibrated with an NREL calibrated KG3 filtered Si reference cell. The mismatch factor was calculated to be less than 2%, and this mismatch correction was applied to achieve the equivalent of 100 mWcm<sup>2</sup> AM1.5 irradiance for the 1 sun measurements. Details are presented in the method section and Supplementary Notes. This same reference cell was used to calibrate the variable intensity under concentrated sun light, with an individual mismatch factor estimation applied for every intensity.

Calculation of spectral mismatch between the reference cell and the devices under test

Yes  
 No

Fully described in the Supplementary Notes.

## 6. Mask/aperture

Size of the mask/aperture used during testing

Yes  
 No

For the standard-area devices, we employed an opaque mask of 0.0919 cm<sup>2</sup> metal aperture to define the active area and to eliminate edge effects. The electronic active area of the cell, as defined by the overlap of the FTO electrode and metal electrode, was ~ 0.12cm<sup>2</sup>. For the small-area CPV devices, no mask/aperture was used since the error is shadowing and area estimation of the small area masks is very high. Instead, as we clearly describe in the manuscript, we used the J<sub>sc</sub> measured on the properly masked and mismatch corrected standard size cell to "self-calibrate" the J<sub>sc</sub> and equivalent active area on the small area cell. The small area cell is created by mechanically scribing the same standard area cell. A full description is given in the supplementary information.

Variation of the measured short-circuit current density with the mask/aperture area

Yes  
 No

We present JV curves for a standard area and a small area cells in Supplementary Fig. 3.

## 7. Performance certification

Identity of the independent certification laboratory that confirmed the photovoltaic performance

Yes  
 No

No calibration lab appears to be offering concentrator measurements on Perovskite solar cells at present.

A copy of any certificate(s)

*Provide in Supplementary Information*

Yes  
 No

*Explain why this information is not reported/not relevant.*

## 8. Statistics

Number of solar cells tested

Yes  
 No

We have tested multiple tens of cells. In Fig. 2 we show the statistics for 8 cells.

Statistical analysis of the device performance

Yes  
 No

We give statistical characteristics of the device performance in Fig. 2.

## 9. Long-term stability analysis

Type of analysis, bias conditions and environmental conditions

*For instance: illumination type, temperature, atmosphere humidity, encapsulation method, preconditioning temperature*

Yes  
 No

We performed aging tests on devices under 10 suns using a xenon lamp simulated full spectrum AM 1.5 G simulator. The device is held at maximum power point (MPP) during aging and kept at a constant temperature by an air stream flowing onto the devices (FTO side), with the device surface measuring approximately 30 oC. All measurements were performed on encapsulated cells in ambient air. We give full details in Fig.4 and the method section.